Nanoscale

PAPER

View Article Online
View Journal | View Issue

Cite this: *Nanoscale*, 2016, **8**, 9714

Anisotropic mechanoresponse of energetic crystallites: a quantum molecular dynamics study of nano-collision†

Ying Li,*[a,b] Rajiv K. Kalia,[b] Masaaki Misawa,[b,c] Aiichiro Nakano,[b] Ken-ichi Nomura,[b] Kohei Shimamura,[b,c,d] Fuyuki Shimojo[c] and Priya Vashishta[b]

Received 10th December 2015,
Accepted 12th April 2016

DOI: 10.1039/c5nr08769d

www.rsc.org/nanoscale

At the nanoscale, chemistry can happen quite differently due to mechanical forces selectively breaking the chemical bonds of materials. The interaction between chemistry and mechanical forces can be classified as mechanochemistry. An example of archetypal mechanochemistry occurs at the nanoscale in anisotropic detonating of a broad class of layered energetic molecular crystals bonded by inter-layer van der Waals (vdW) interactions. Here, we introduce an *ab initio* study of the collision, in which quantum molecular dynamic simulations of binary collisions between energetic vdW crystallites, TATB molecules, reveal atomistic mechanisms of anisotropic shock sensitivity. The highly sensitive lateral collision was found to originate from the twisting and bending to breaking of nitro-groups mediated by strong intra-layer hydrogen bonds. This causes the closing of the electronic energy gap due to an inverse Jahn–Teller effect. On the other hand, the insensitive collisions normal to multilayers are accomplished by more delocalized molecular deformations mediated by inter-layer interactions. Our nano-collision studies provide a much needed atomistic understanding for the rational design of insensitive energetic nanomaterials and the detonation synthesis of novel nanomaterials.

Introduction

The rational design of materials is possible due to advancements in recent experimental techniques, in which chemical reactions are controlled mechanically.[1–4] In so-called mechanochemistry, mechanical forces selectively break covalent bonds. Such mechanochemistry can now be studied at the nanoscale with recently developed theoretical nanoreactors[5] and nanoscale impact experiments.[6] An illustration is the application of sonication of polymers, where polymers exhibit different reaction pathways when exposed to ultrasound than when exposed to light or heat.[7] Another prime example is the detonation of energetic materials, where mechanical shock waves initiate exothermic reactions to self-sustain wave propagation.[8,9] In typical energetic molecular crystals, it takes only 10^{-13} s (*i.e.*, the period of one molecular vibration) for a detonation wave front to pass through each molecule. This timescale is too short for chemical reactions to be thermally activated. Consequently, the reactions are likely to be initiated athermally *via* mechanical activation.[10] An archetypal example of mechanochemistry appears during the detonation of triaminotrinitrobenzene (TATB) or 2,4,6-triamino-1,3,5-trinitrobenzene. It was suggested theoretically that mechanical bending of a nitrate group in a TATB molecule closes the energy gap between the highest occupied molecular orbital (HOMO) and the lowest unoccupied molecular orbital (LUMO) through an inverse Jahn–Teller effect.[10,11] The closing of the HOMO–LUMO gap liberates bonding electrons to initiate chemical reactions.

TATB fits into the category of layered energetic molecular crystals, which are extremely insensitive to shock or impact. Due to the reduced likelihood of accidental detonation, TATB is favoured for applications in safety engineering.[12] The inter-layer van der Waals (vdW) interactions[13–16] hold together the layered crystal structure of TATB molecules, which is similar to the structures of vdW materials that are gaining growing attention due to their unique physical and chemical properties.[17,18] Within each layer, on the other hand, these energetic crystals are inter-bonded by a strong hydrogen-bond network in addition to intra-molecular covalent bonds. The interplay between inter-layer vdW forces and intra-layer hydrogen bonds

[a]*Argonne Leadership Computing Facility, Argonne National Laboratory, Argonne, Illinois 60439, USA. E-mail: yingli@anl.gov; Tel: +1-630-252-3394*
[b]*Collaboratory for Advanced Computing and Simulations, Department of Physics and Astronomy, Department of Computer Science, Department of Chemical Engineering and Material Science, University of Southern California, Los Angeles, California 90089-0242, USA*
[c]*Department of Physics, Kumamoto University, Kumamoto 860-8555, Japan*
[d]*Graduate School of System Informatics, Kobe University, Kobe 657-8501, Japan*
†Electronic supplementary information (ESI) available. See DOI: 10.1039/c5nr08769d

is expected to dictate the anisotropic detonation behaviours of these energetic vdW crystals. A fundamental scientific question is: how does the interplay between vdW forces and hydrogen bonds determine the anisotropic mechanochemistry in energetic vdW crystals? Recent nanoscale impact experiments have studied the mechanical responses of multilayer vdW materials,[6] and similar mechanochemical anisotropy was studied previously using the binary collision of pentaerythritol tetranitrate (PETN) molecules.[19,20] However, such bi-molecular collision cannot capture the inter-layer/intra-layer effects of interest. To address this key issue, we here introduce an *ab initio* study of collision, in which the collision of TATB crystallites is studied using quantum molecular dynamics (QMD) simulations.[21–24] QMD follows the trajectories of all atoms while computing the interatomic interactions quantum mechanically based on density functional theory (DFT).[25] Our nanocollider augments recently developed nanoreactor[5] and nanoscale impact[6] technologies, thereby providing not only an interpretation of experimental findings but also the discovery of new reaction pathways.

Simulation methods

TATB is a rather intensive aromatic explosive, based on the basic six-carbon benzene ring structure with three nitro functional groups (NO_2) and three amine (NH_2) groups attached, alternating around the ring.[26–28] There are two TATB molecules in each triclinic unit cell[29] with lattice parameters of a = 9.01 Å, b = 9.028 Å, c = 6.812 Å, α = 108.58°, β = 91.82°, and γ = 119.97° (Fig. 1(a)). The initial simulation box consists of a TATB crystalline unit cell repeated 2 × 2 × 2 times in the a, b and c crystallographic directions with 20 Å of extra space added along each direction (Fig. 1(b)). To study the crystalline anisotropy in TATB, we perform two sets of simulations. This amounts to a collision speed of 6 km s^{-1}, which is slightly below the detonation speed of TATB crystals.[30] In total, we have six different systems set up for 6 km s^{-1} a-axis and c-axis collisions (three trajectories for each collision). Each uses different random seeds for initiating velocity for atoms and wave functions for electrons: by assigning opposing initial velocities of 3 km s^{-1} to two crystallites, each containing 8 molecules, the crystallites collide along the a-axis (Fig. 1(c)) and c-axis (Fig. 1(d)) directions, respectively.

In our QMD simulations, the electronic states are calculated using the projector-augmented-wave (PAW) method.[31] The generalized gradient approximation (GGA),[32] along with vdW correction,[33] is used for the exchange–correlation energy with non-linear core corrections based on the DFT-D method.[34] The momentum-space formalism is utilized, where the plane-wave cutoff energies are 30 and 250 Ry for electronic pseudo-wave functions and pseudo-charge density, respectively, and the gamma point is used in the Brillouin zone. The energy functional is minimized iteratively using a preconditioned conjugated gradient method. Projector functions are generated for the 2s and 2p states of C, N and O, and for the 1s state for H. Our QMD code has been implemented on parallel computers by a hybrid approach combining spatial decomposition (*i.e.*, distributing real-space or reciprocal-space grid points among processors) and band decomposition (*i.e.*, assigning the calculations of different Kohn–Sham orbitals to different processors).[24,35] A quasi-Newton method is used for structural optimization prior to the QMD simulations. The QMD simulations are carried out using interatomic forces that are computed quantum mechanically based on the Hellmann–Feynman theorem. The equations of motion are integrated numerically with a time step of 10 a.u. (~0.24 fs).

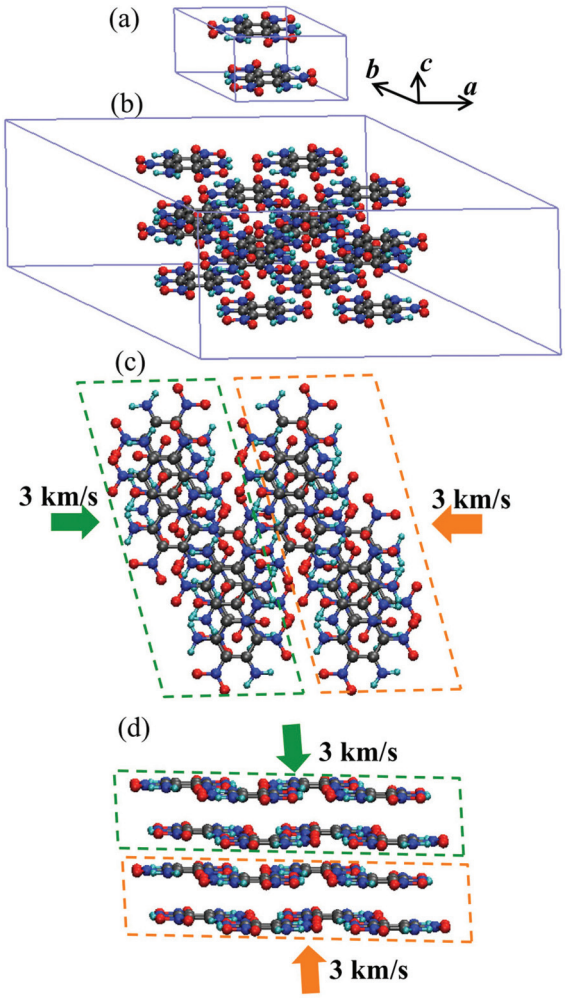

Fig. 1 Simulated TATB nanocrystallites. (a) The TATB molecular crystal unit cell structure, (b) the simulation box containing 16 TATB molecules. (c) Schematic of the a-axis collision, where two crystallites enclosed respectively by green and orange dashed lines collide with speeds of 3 km s^{-1} indicated by the arrows. (d) The same as shown in (c), but for the c-axis collision.

Results

To study the chemical reaction pathways, we perform fragment analysis, where a cluster of covalently bonded atoms is

counted as a fragment. Here a pair of atoms is considered connected if their distance is shorter than a critical value, but is slightly longer than the corresponding covalent bond length. Fig. 2(a) and (b) show the number of fragments as a function of time for the *a*-axis and *c*-axis collisions, respectively. In the case of the *a*-axis collision, Fig. 2(a) shows the number of fragments with a reasonable amount of statistical discrepancy, but with overall consistency for different trajectories, for example, a number of NO_2 fragments are produced as shown in Fig. 2(a). In contrast, Fig. 2(b) shows no bond breakage for the *c*-axis collision. These results indicate that the *a*-axis collision is more sensitive compared with the *c*-axis collision. The production of NO_2 as the initial reaction product is consistent with the case of the bi-molecular collision in PETN[19] and the shock-induced detonation of cyclotrimethylenetrinitramine (RDX) crystals.[36–38]

The anisotropic sensitivity shown above is also reflected in the temperature of the system. To compute the temperature, we take account of the average kinetic energy of the atoms in each individual fragment by subtracting the center-of-mass velocity of the fragment from the velocity of each atom for every trajectory (the concept of temperature is different from the thermal average of the kinetic energy of a solid-state system, because the time scale is too short for chemical reactions to be thermally activated). Fig. 2(c) and (d) show the temperatures of the six systems as a function of time. For the *a*-axis collision, the temperature generally rises rapidly and reaches 1350 K by the end of the simulation (Fig. 2(c)). On the other hand, for the *c*-axis collision, the temperature generally exhibits a periodic oscillation reflecting multiple collisions among the TATB layers (Fig. 2(d)). The temperature for the *c*-axis collision remains around 1000 K, which is much lower than that in the *a*-axis collision. The more rapid temperature rise in the *a*-axis collision indicates that the kinetic energy of the colliding crystallites is converted to molecular vibrational modes more effectively compared to the *c*-axis collision.[39] The different temperatures between Fig. 2(c) and (d) arise from the very different intermediate chemical reactions between the *a*-axis and *c*-axis collisions within 100 fs, illustrated, *e.g.*, by the different intermediate products shown in Fig. 2(a) and (b). Consequently, different amounts of energy are released, thereby resulting in different temperatures. This is a manifestation of the mechanochemical initiation of chemical reactions, which is highly sensitive to molecular shapes and

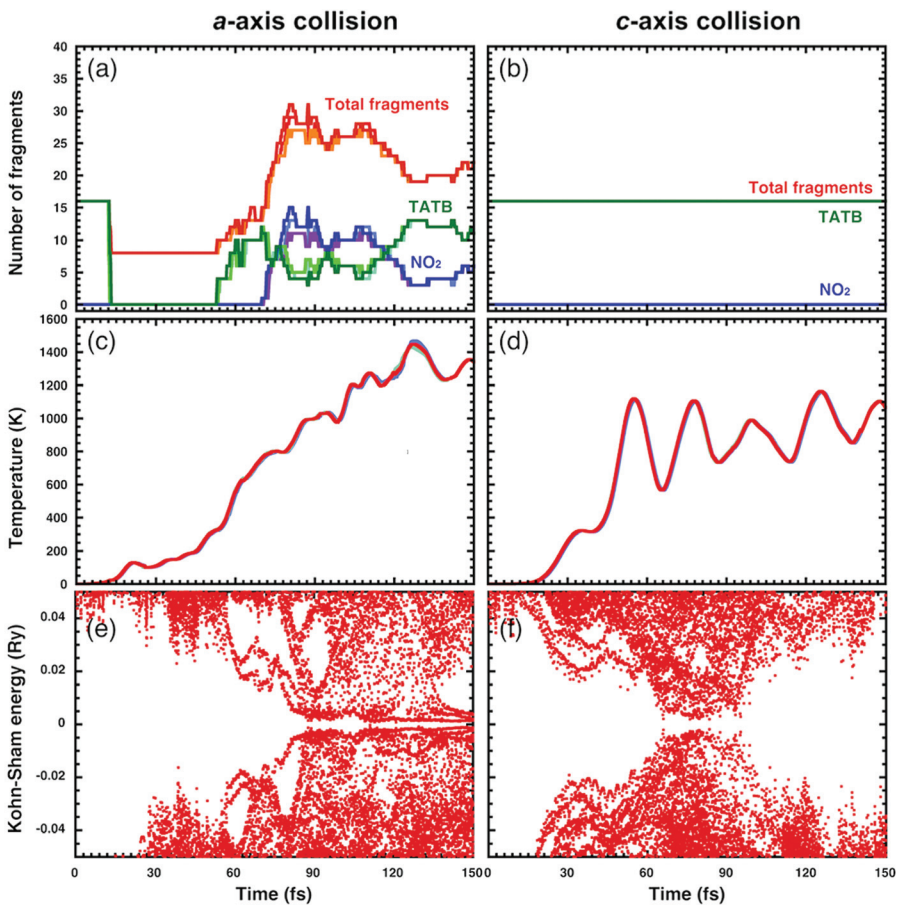

Fig. 2 Time evolution of the *a*- and *c*-axis collision simulations. (a) and (b) show the number of molecular fragments, (c) and (d) show the temperature, and (e) and (f) show the Kohn–Sham eigenenergies. The left and right columns are for the *a*-axis and *c*-axis collisions, respectively, each with three different trajectories. Also see Fig. S1† for details of the Kohn–Sham eigenenergies for the additional trajectories.

crystallographic packing. As all of the systems complete reactions to produce the same final products, however, they should reach the same thermodynamic state. According to previous simulations on TATB[27] and related energetic molecular crystals,[38] this is expected to take longer than ns.

Fig. 2(e) and (f) plot the electronic Kohn–Sham eigenenergies as a function of time for one of the *a*-axis and *c*-axis collisions, respectively (the other four trajectories also show similar looking Kohn–Sham eigenenergies as a function of time for 6 km s^{-1} *a*- and *c*-axis collisions, see also Fig. S1(a)–(d), in ESI,† for details). In Fig. 2(e) for the *a*-axis collision, the HOMO–LUMO energy gap closes at around 80 fs and remains closed for the entire simulation. In the *c*-axis collision, the HOMO–LUMO gap also closes at around 80 fs. However, the gap reopens as the two crystallites bounce back after the *c*-axis collision (Fig. 2(f)) in a sharp contrast to the *a*-axis collision where the gap remains closed (Fig. 2(e)). An energy-gap closure similar to those in Fig. 2(e) and (f) was observed in DFT calculations of a single TATB molecule by Manaa.[11] His calculation identifies the closure of the energy gap due to the bending of the nitro-group. As shown below, the gap closure in our simu-

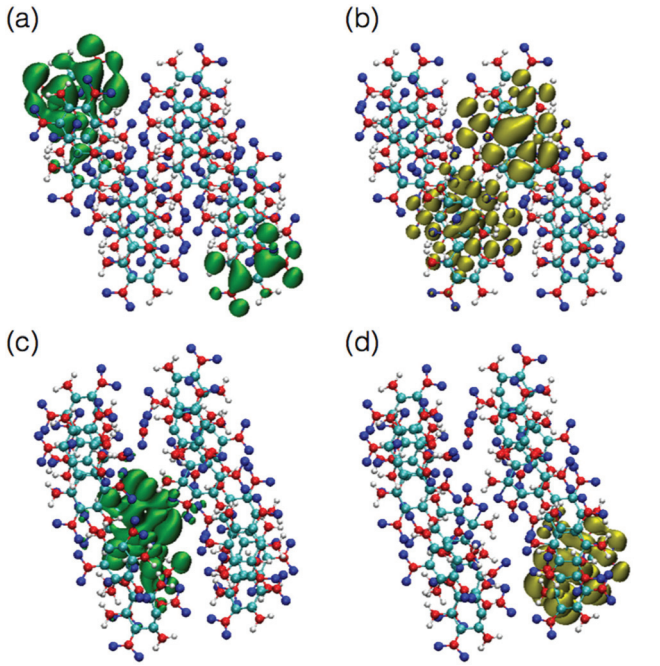

Fig. 3 HOMO and LUMO electron densities during the *a*-axis collision before and after the band gap closure. Isosurfaces are shown for (a) the HOMO before gap closure, (b) the LUMO before gap closure, (c) the HOMO after gap closure, and (d) the LUMO after gap closure.

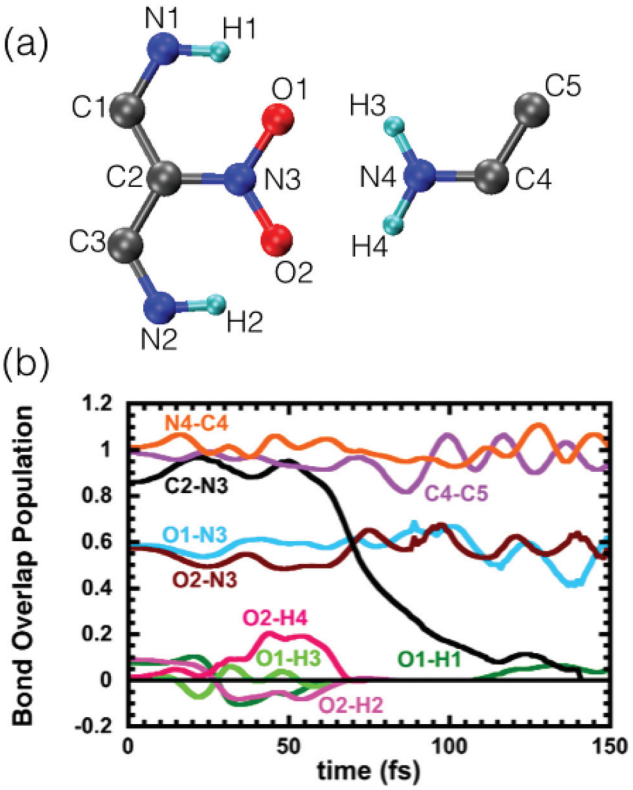

Fig. 5 Chemical bond dynamics. (a) Key atoms involved in one of the NO_2 dissociation reactions in the *a*-axis collision. (b) Bond overlap population between key atomic pairs involved in the reaction.

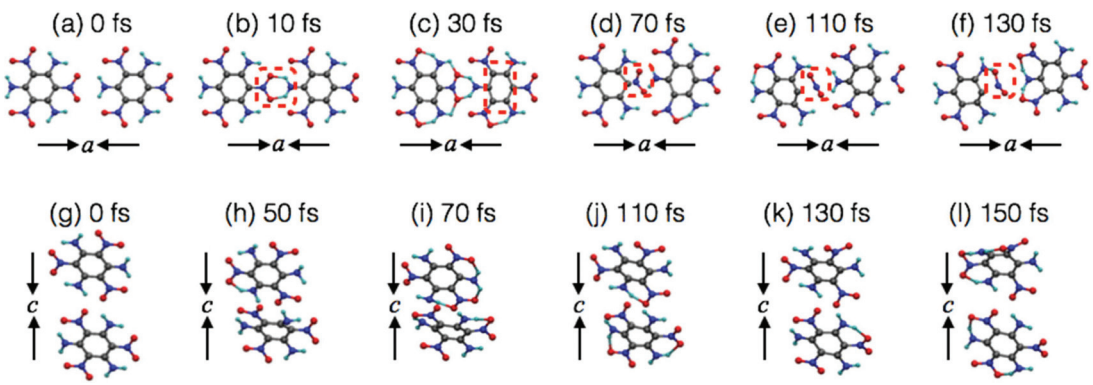

Fig. 4 Atomistics of the anisotropic collisions. Snapshots of the *a*-axis ((a)–(f)) and *c*-axis ((g)–(l)) collision simulations. The cyan, gray, blue and red spheres represent H, C, N and O atoms, respectively.

lation is accompanied by the twisting and bending of nitro-groups, which is consistent with the results by Manaa.[11] The energy degeneracy caused by molecular distortion can be viewed as an inverse Jahn–Teller effect. Here geometrical distortion from the ground state causes the destabilization of the electronic structures (*i.e.*, a closing of the HOMO–LUMO gap), which in turn causes the liberation of frontier orbitals to promote chemical reactions.[10,11] Fig. 3 shows the electronic charge densities of the highest occupied molecular orbital (HOMO) and lowest unoccupied molecular orbital (LUMO) before (0 fs) and after (150 fs) the band gap closure during the *a*-axis collision.

To contrast the different reaction mechanisms in the *a*- and *c*-axis collisions, the snapshots in Fig. 4 show part of the two simulation systems (see also movies, S1.mov and S2.mov, in ESI†). Fig. 4(a)–(f) for the *a*-axis collision show the production of NO_2 from a TATB molecule. At 10 fs, strong inter-molecular hydrogen bonds are formed between two adjacent TATB molecules (Fig. 4(b)). At 30 fs, the carbon ring in one of the TATB molecules (on the right in Fig. 4(c)) deforms severely due to the contact with another TATB molecule (on the left in Fig. 4(c)). As the carbon ring restores its shape, the inter-molecular hydrogen bonds cause twisting and bending of the NO_2 group at the collision front in the left TATB molecule (Fig. 4(d) and (e)). This causes the scission of the C–N bond, and the dissociation of an NO_2 molecule (Fig. 4(e) and (f)). On the contrary, no reaction is observed in Fig. 4(g)–(l) for the *c*-axis collision. As TATB molecules approach each other in the *c*-axis collision, hydrogen bonds are formed only within individual TATB molecules in contrast to the formation of inter-molecular hydrogen bonds during the *a*-axis collision. The marked difference can be understood as follows. In the *a*-axis collision, the two inter-molecular hydrogen bonds push and twist one of the NO_2 groups in the left TATB molecule (Fig. 4(b) and (c)). Here, there is only one C–N bond connecting the NO_2 group to the carbon. On the contrary, in the *c*-axis collision, the mechanical load is shared by a more delocalized deformation of the entire molecule, which is not sufficient to break any covalent bond.

To quantify the NO_2 dissociation in the *a*-axis collision, we perform a bond overlap population (BOP) analysis[40] by expanding the electronic wave functions with an atomic-orbital basis set.[41] Based on the formulation generalized to the PAW method,[21–23] we obtain the gross population Z_i for the i^{th} atom and the BOP O_{ij} for the pair of i^{th} and j^{th} atoms. From Z_i, we estimate the atomic charge, and O_{ij} gives a semi-quantitative estimate of the strength of covalent bonding. As for the atomic basis orbitals, we use numerical eigenfunctions of atoms,

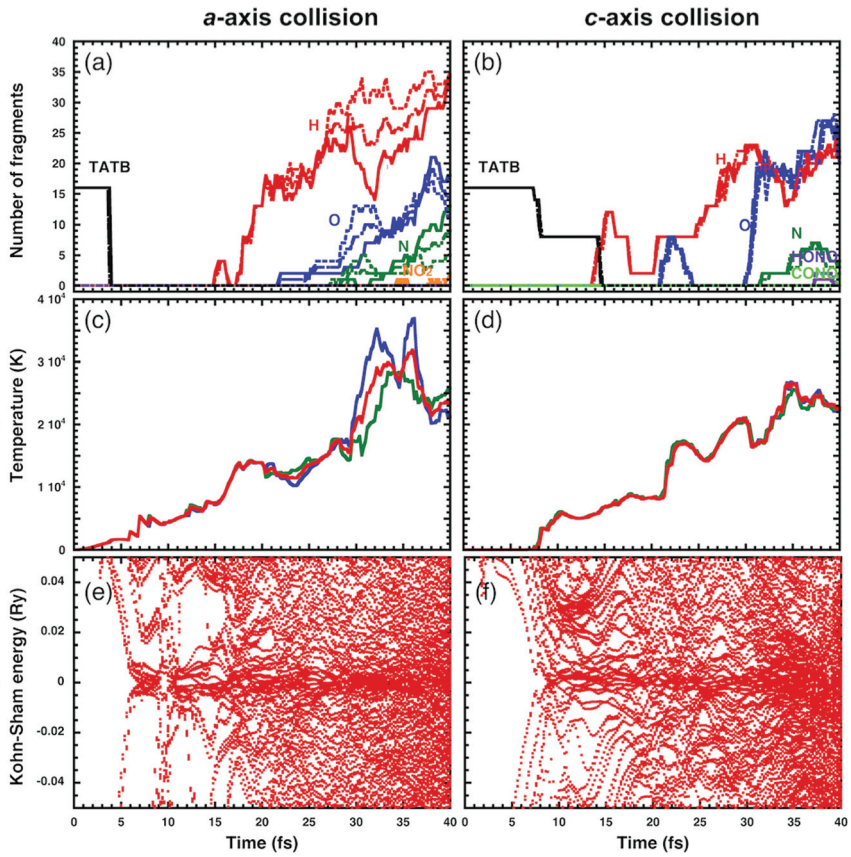

Fig. 6 Time evolution of the *a*- and *c*-axis collision simulations with a speed of 20 km s^{-1}. (a) and (b) show the number of molecular fragments, (c) and (d) show the temperature, and (e) and (f) show the Kohn–Sham eigenenergies. The left and right columns are for the *a*-axis and *c*-axis collisions, respectively, each with three different trajectories. Also see Fig. S2† for the details of Kohn–Sham eigenenergies for the additional trajectories.

which are obtained from a chosen atomic energy so that the first node coincides with the desired cutoff radius.[42] To increase the efficiency of the expansion, the numerical basis orbitals are augmented with the split-valence method.[43] The resulting charge spillage, which estimates the error in the expansion, is only 0.2%, indicating the high quality of the basis orbitals.

Fig. 5(a) shows the key atoms involved in one of the NO_2 dissociation reactions, while Fig. 5(b) shows the time evolution of the BOP between them. Fig. 5(b) shows the gradual breakage of a CN bond (labelled C2–N3) at around 70–140 fs. The formation of a strong inter-molecular hydrogen bond (*i.e.*, O2–H4 at around 30–70 fs) indeed precedes the C–N scission as discussed above. Despite the loss of BOP between C2 and N3, no other pair shows a clear increase of BOP to compensate for it. This reflects a rather delocalized transfer of electrons across many atoms.

It should be noted here that the transient HOMO–LUMO gap closing observed near the collision front in our simulation is distinct from bulk metallization under homogeneous deformation over much longer space and time scales. Under homogeneous compression, both experiments[44] and DFT calculations[45] show the absence of bulk metallization below a pressure of 100 GPa. The transient, heterogeneous gap closing found in our simulation occurs within 10^{-13} s after the collision or within 10^{-9} m from the collision front. This is exactly the athermal mechanochemical spatiotemporal regime expected for the inverse Jahn–Teller effect.[1,10] Subsequently, the energy gap should reopen as the molecular fragments relax to their local minimum-energy configurations.

In order to understand the anisotropic reactions initiated at such hot spots, we have performed another six sets of simulations at a higher collision speed of 20 km s^{-1}, which is above the detonation speed of TATB crystals. Fig. 6 shows the comparison of the number of fragments, temperature and Kohn–Sham eigenenergies for the *a*- and *c*-axis collisions.[39] Fig. 6(a) and (b) show that most of the fragments of the *a*- and *c*-axis collisions (three trajectories for each collision) during the collision at 20 km s^{-1} are atomized atoms, such as H, O and N. In addition, some NO_2 fragments are found at the end of the *a*-axis collision. On the other hand, HONO and CONO molecules are observed in the *c*-axis collision. The temperatures in Fig. 6(c) and (d) show that the *a*-axis collision produces more heat than the *c*-axis collision. The very rapid closing of the HOMO–LUMO gap in both *a*- and *c*-axis collisions is shown in Fig. 6(e) and (f) (four more trajectories also show similar looking Kohn–Sham eigenenergies as a function of time for 20 km s^{-1} *a*- and *c*-axis collisions, see the details in Fig. S2(a)–(d), in ESI†). Overall, crystalline anisotropy very similar to that in the 6 km s^{-1} collision persists up to much higher velocities.

Conclusions

The atomistic understanding obtained by our nanocollider may pave a way toward the rational design of insensitive energetic nanomaterials[46] and detonation synthesis of novel nanomaterials, such as nanodiamond.[47] Our QMD simulations identify specific events, and their molecular origins, that initiate chemical reactions under shock. Specifically, the present simulations suggest the avoidance of localized load-bearing motifs (*e.g.*, a small number of interlayer N–N contacts) for the design of more insensitive energetic materials. QMD simulations dynamically follow reaction pathways and are thereby able to predict unique reaction products.

Acknowledgements

This work was supported by the Air Force Office of Scientific Research Grant No. FA9550-16-1-0042. Simulations were performed at the Center for High-Performance Computing of the University of Southern California. We appreciate the Margaret Butler Postdoctoral Fellowship at Argonne Leadership Computing Facility for supporting of the work.

References

1 J. J. Gilman, *Science*, 1996, **274**, 65–65.
2 D. A. Davis, A. Hamilton, J. L. Yang, L. D. Cremar, D. Van Gough, S. L. Potisek, M. T. Ong, P. V. Braun, T. J. Martinez, S. R. White, J. S. Moore and N. R. Sottos, *Nature*, 2009, **459**, 68–72.
3 J. N. Brantley, K. M. Wiggins and C. W. Bielawski, *Science*, 2011, **333**, 1606–1609.
4 B. A. Beiermann, S. L. B. Kramer, J. S. Moore, S. R. White and N. R. Sottos, *ACS Macro Lett.*, 2012, **1**, 163–166.
5 L. P. Wang, A. Titov, R. McGibbon, F. Liu, V. S. Pande and T. J. Martinez, *Nat. Chem.*, 2014, **6**, 1044–1048.
6 J. H. Lee, P. E. Loya, J. Lou and E. L. Thomas, *Science*, 2014, **346**, 1092–1096.
7 C. R. Hickenboth, J. S. Moore, S. R. White, N. R. Sottos, J. Baudry and S. R. Wilson, *Nature*, 2007, **446**, 423–427.
8 D. W. Brenner, D. H. Robertson, M. L. Elert and C. T. White, *Phys. Rev. Lett.*, 1993, **70**, 2174–2177.
9 E. J. Reed, M. R. Manaa, L. E. Fried, K. R. Glaesemann and J. D. Joannopoulos, *Nat. Phys.*, 2008, **4**, 72–76.
10 J. J. Gilman, *Mater. Sci. Technol.*, 2006, **22**, 430–437.
11 M. R. Manaa, *Appl. Phys. Lett.*, 2003, **83**, 1352–1354.
12 V. M. Boddu, D. S. Viswanath, T. K. Ghosh and R. Damavarapu, *J. Hazard. Mater.*, 2010, **181**, 1–8.
13 Z. F. Wang, Q. X. Li, H. B. Su, X. P. Wang, Q. W. Shi, J. Chen, J. L. Yang and J. G. Hou, *Phys. Rev. B: Condens. Matter*, 2007, **75**, 085424.
14 D. Le, A. Kara, E. Schroder, P. Hyldgaard and T. S. Rahman, *J. Phys.: Condens. Matter*, 2012, **24**, 424210.
15 L. M. Liu, R. Car, A. Selloni, D. M. Dabbs, I. A. Aksay and R. A. Yetter, *J. Am. Chem. Soc.*, 2012, **134**, 19011–19016.
16 B. B. Averkiev, Z. A. Dreger and S. Chaudhuri, *J. Phys. Chem. A*, 2014, **118**, 10002–10010.

17 B. Hunt, J. D. Sanchez-Yamagishi, A. F. Young, M. Yankowitz, B. J. LeRoy, K. Watanabe, T. Taniguchi, P. Moon, M. Koshino, P. Jarillo-Herrero and R. C. Ashoori, *Science*, 2013, **340**, 1427–1430.
18 A. K. Geim and I. V. Grigorieva, *Nature*, 2013, **499**, 419–425.
19 C. J. Wu, F. H. Ree and C. S. Yoo, *Propellants, Explos., Pyrotech.*, 2004, **29**, 296–303.
20 A. C. Landerville, I. I. Oleynik and C. T. White, *J. Phys. Chem. A*, 2009, **113**, 12094–12104.
21 F. Shimojo, S. Ohmura, R. K. Kalia, A. Nakano and P. Vashishta, *Phys. Rev. Lett.*, 2010, **104**, 126102.
22 K. Shimamura, F. Shimojo, R. K. Kalia, A. Nakano and P. Vashishta, *Phys. Rev. Lett.*, 2013, **111**, 066103.
23 K. Shimamura, F. Shimojo, R. K. Kalia, A. Nakano, K. Nomura and P. Vashishta, *Nano Lett.*, 2014, **14**, 4090–4096.
24 N. A. Romero, A. Nakano, K. M. Riley, F. Shimojo, R. K. Kalia, P. Vashishta and P. C. Messina, *Computer*, 2015, **48**, 33–41.
25 P. Hohenberg and W. Kohn, *Phys. Rev.*, 1964, **136**, B864–B871.
26 L. Z. Zhang, S. V. Zybin, A. C. T. van Duin, S. Dasgupta, W. A. Goddard and E. M. Kober, *J. Phys. Chem. A*, 2009, **113**, 10619–10640.
27 M. R. Manaa, E. J. Reed, L. E. Fried and N. Goldman, *J. Am. Chem. Soc.*, 2009, **131**, 5483–5487.
28 D. E. Taylor, *J. Phys. Chem. A*, 2013, **117**, 3507–3520.
29 R. H. Gee, S. Roszak, K. Balasubramanian and L. E. Fried, *J. Chem. Phys.*, 2004, **120**, 7059–7066.
30 T. Tran, C. Tarver, J. Maienschein, P. Lewis, M. Moss, R. Druce, R. Lee and F. Roeske, *12th International Detonation Symposium Proceedings*, 2002.
31 P. E. Blochl, *Phys. Rev. B: Condens. Matter*, 1994, **50**, 17953–17979.
32 J. P. Perdew, K. Burke and M. Ernzerhof, *Phys. Rev. Lett.*, 1996, **77**, 3865–3868.
33 S. Grimme, *J. Comput. Chem.*, 2006, **27**, 1787–1799.
34 S. G. Louie, S. Froyen and M. L. Cohen, *Phys. Rev. B: Condens. Matter*, 1982, **26**, 1738–1742.
35 F. Shimojo, S. Hattori, R. K. Kalia, M. Kunaseth, W. W. Mou, A. Nakano, K. Nomura, S. Ohmura, P. Rajak, K. Shimamura and P. Vashishta, *J. Chem. Phys.*, 2014, **140**, 18A529.
36 K. I. Nomura, R. K. Kalia, A. Nakano, P. Vashishta, A. C. T. van Duin and W. A. Goddard, *Phys. Rev. Lett.*, 2007, **99**, 148303.
37 A. Strachan, A. C. T. van Duin, D. Chakraborty, S. Dasgupta and W. A. Goddard, *Phys. Rev. Lett.*, 2003, **91**, 098301.
38 Y. Li, R. K. Kalia, A. Nakano, K. I. Nomura and P. Vashishta, *Appl. Phys. Lett.*, 2014, **105**, 204103.
39 D. D. Dlott, in *Overviews of Recent Research on Energetic Materials*, ed. R. W. Shaw, T. B. Brill and D. L. Thompson, World Scientific, Singapore, 2005, vol. 16, pp. 303–333.
40 R. S. Mulliken, *J. Chem. Phys.*, 1955, **23**, 1833–1840.
41 M. D. Segall, R. Shah, C. J. Pickard and M. C. Payne, *Phys. Rev. B: Condens. Matter*, 1996, **54**, 16317–16320.
42 O. F. Sankey and D. J. Niklewski, *Phys. Rev. B: Condens. Matter*, 1989, **40**, 3979–3995.
43 J. M. Soler, E. Artacho, J. D. Gale, A. Garcia, J. Junquera, P. Ordejon and D. Sanchez-Portal, *J. Phys: Condens. Matter*, 2002, **14**, 2745–2779.
44 A. J. Davidson, R. P. Dias, D. M. Dattelbaum and C. S. Yoo, *J. Chem. Phys.*, 2011, **135**, 174507.
45 C. J. Wu, L. H. Yang, L. E. Fried, J. Quenneville and T. J. Martinez, *Phys. Rev. B: Condens. Matter*, 2003, **67**, 235101.
46 Z. Wang, X. Guo, F. Wu and T. Yan, *Propellants, Explos., Pyrotech.*, 2016, **41**, 327–333.
47 V. Pichot, B. Risse, F. Schnell, J. Mory and D. Spitzer, *Sci. Rep.*, 2013, **3**, 2159.

